Tuning ferromagnetism at room temperature by visible light

Bálint Náfrádi[a,1], Péter Szirmai[a], Massimo Spina[a], Andrea Pisoni[a], Xavier Mettan[a], Norbert M. Nemes[b,c], László Forró[a,1], and Endre Horváth[a]

[a]Laboratory of Physics of Complex Matter, Ecole Polytechnique Fédérale de Lausanne, CH-1015 Lausanne, Switzerland; [b]GFMC, Departamento de Fisica de Materiales, Universidad Complutense de Madrid, 28040 Madrid, Spain; and [c]Unidad Asociada ICMM-CSIC "Laboratorio de Heteroestructuras con Aplicacion en Espintronica," Consejo Superior de Investigaciones Cientificas, 28049 Madrid, Spain

Edited by Myriam P. Sarachik, The City College of the City University of New York, New York, NY, and approved January 22, 2020 (received for review September 10, 2019)

Most digital information today is encoded in the magnetization of ferromagnetic domains. The demand for ever-increasing storage space fuels continuous research for energy-efficient manipulation of magnetism at smaller and smaller length scales. Writing a bit is usually achieved by rotating the magnetization of domains of the magnetic medium, which relies on effective magnetic fields. An alternative approach is to change the magnetic state directly by acting on the interaction between magnetic moments. Correlated oxides are ideal materials for this because the effects of a small external control parameter are amplified by the electronic correlations. Here, we present a radical method for reversible, light-induced tuning of ferromagnetism at room temperature using a halide perovskite/oxide perovskite heterostructure. We demonstrate that photoinduced charge carriers from the $CH_3NH_3PbI_3$ photovoltaic perovskite efficiently dope the thin $La_{0.7}Sr_{0.3}MnO_3$ film and decrease the magnetization of the ferromagnetic state, allowing rapid rewriting of the magnetic bit. This manipulation could be accomplished at room temperature; hence this opens avenues for magnetooptical memory devices.

LSMO | $CH_3NH_3PbI_3$ | magnetism tuning | heat-assisted magnetic recording

Chemical doping offers, undisputedly, the broadest tuning range of electronic and magnetic properties of correlated oxides. For instance, 30% substitution of Sr to the La sites changes the antiferromagnetic insulator $LaMnO_3$ to a ferromagnetic metal with Curie temperature (T_C) exceeding room temperature (Fig. 1*A*) (1, 2). The ferromagnetic state of doped $La_{1-x}Sr_xMnO_3$ (LSMO) with finely-tuned chemical composition has a high sensitivity to external magnetic fields in the vicinity of the magnetic phase transition showing colossal magnetoresistance (CMR) (3). However, producing locally-focused strong magnetic fields is challenging and not very energy-efficient. Novel methods for improving the characteristics rely on heterostructures where the interaction between the distinctive constituents results in new functionality. For instance, in $LaAlO_3/SrTiO_3$ heterostructure, correlated electron phenomena, such as superconductivity and ferromagnetism, emerge at the interface (4–6). The sensitivity of the magnetic state of LSMO to structural changes is well known and allows in situ modification of the magnetic structure via strain in LSMO/$BaTiO_3$ heterostructure using the piezoelectricity of $BaTiO_3$ (7). A more straightforward approach to modulate the magnetic state is to directly change the carrier concentration of LSMO by means of an electric field, which can be sizable in thin films. Indeed, field effect transistor geometries offer electronic tuning of T_C in an $La_{0.825}Sr_{0.175}MnO_3/Pb_{0.2}Zr_{0.8}TiO_3$ heterostructure (8). In addition to solid-state heterostructures, electronic double layers appearing at the liquid electrode/LSMO interfaces were also used to manipulate magnetism (6, 9–11). These methods take advantage of the high electric field that develops at the interface and thus shifts the Fermi level of LSMO (12). All of these methods offer very rich physics, but their applicability in devices is less clear. Ultrafast all-optical switching of magnetism and photomagnetic recording have already been demonstrated in several materials, but these required powerful laser pulses operating at a repetition rate in the megahertz range (13–16).

Transient optical switching of conductivity was also achieved in oxygen-deficient LSMO, taking advantage of electron trapping in oxygen vacancies (17). The trapped electrons can be efficiently released by a magnetic field of <1 T (18). Therein, electron trapping acts through the orbital state of LSMO to modify the magnetism in the crystal.

In a broader context, light illumination-induced charge transfer was found to be a powerful tool to manipulate the material properties. Specifically, the superconducting transition temperature of thin-film high-T_c structures increases substantially through illumination (19, 20).

Advancing these approaches, we present an optical method for in situ tunable doping of LSMO thin films and control of their magnetic and electronic state. We take advantage of the outstanding photoelectron generation capability

Significance

The rise of digitalization led to an exponential increase in demand for data storage. Mass storage is resolved by hard disk drives (HDDs) due to their relatively long lifespan and low price. HDDs use magnetic domains, which are rotated to store and retrieve information. However, an increase in capacity and speed is continuously demanded. We report a method to facilitate the writing of magnetic bits optically. We use a sandwich of a highly light-sensitive ($MAPbI_3$) and a ferromagnetic material (LSMO), where illumination of $MAPbI_3$ drives charge carriers into LSMO and decreases its magnetism. This is a viable alternative to the long-sought-after heat-assisted magnetic recording (HAMR) technology, which would heat up the disk material during the writing process.

Author contributions: B.N., L.F., and E.H. designed research; B.N., P.Sz., M.S., A.P., X.M., N.M.N., and E.H. performed research; N.M.N. and E.H. contributed new reagents/analytic tools; B.N., P.Sz., M.S., A.P., N.M.N., and E.H. analyzed data; and B.N., P.Sz., M.S., A.P., X.M., N.M.N., L.F., and E.H. wrote the paper.

The authors declare no competing interest.

This article is a PNAS Direct Submission.

Data deposition: All of the scripts and all of the experimental data used to produce the figures within this work are available at https://doi.org/10.5281/zenodo.3662206.

[1]To whom correspondence may be addressed. Email: laszlo.forro@epfl.ch or nafradi@yahoo.com.

This article contains supporting information online at https://www.pnas.org/lookup/suppl/doi:10.1073/pnas.1915370117/-/DCSupplemental.

First published March 9, 2020.

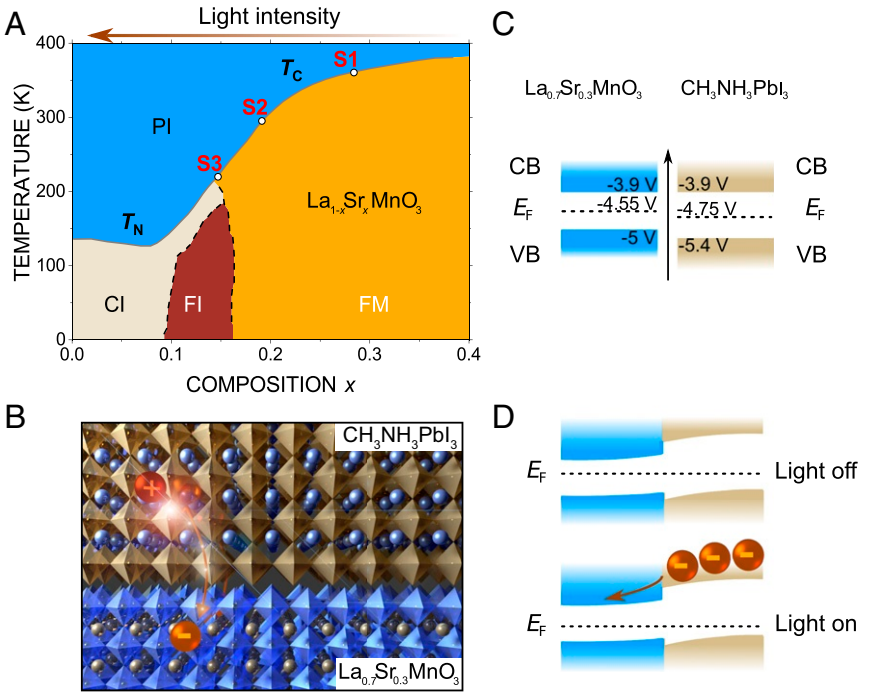

Fig. 1. Light and composition tunable magnetic heterostructures. (*A*) Phase diagram of LSMO as a function of temperature and Sr doping concentration. The abbreviations denote spin-canted insulating (CI), ferromagnetic insulating (FI), ferromagnetic metal (FM), and paramagnetic insulating (PI) phases, and the Néel temperature (T_N). The S1 (film thickness: 29 nm), S2 (14 nm), and S3 (11 nm) dots represent the thin films investigated in the present work with T_C of 350, 310, and 210 K, respectively. The arrow on top indicates the shift in T_C induced by light illumination of the $MAPbI_3$/LSMO heterostructure. (*B*) Schematic representation of the heterostructure. (*C*) Sketch of the band alignment of the measured heterostructure in the insulating phase. The abbreviations denote the conduction band (CB), the valence band (VB), and the Fermi energy (E_F). (*D*) Incoming photon generates an electron–hole pair in the $MAPbI_3$ layer. Due to the chemical potential mismatch, electrons propagate to the LSMO film. The electron diffusion counteracts the chemical doping enforced by the Sr content; thus it changes the Curie temperature (T_C) of the LSMO film.

of methylammonium lead iodide perovskite $CH_3NH_3PbI_3$ (hereafter $MAPbI_3$). In a heterojunction configuration upon light illumination, $MAPbI_3$ transfers photoelectrons to the adjacent LSMO and thus shifts its carrier concentration and the T_C. With this method, by choosing an appropriate temperature and light intensity in the vicinity of T_C, we can freely tune the magnetization of LSMO. A great advantage of this heterostructure is that, depending on the LSMO composition (Fig. 1*A*), the T_C, and hence the magnitude and temperature of the effect on the magnetization, can be tuned at will. For example, the effective magnetization change $\Delta M_{\text{eff}} \equiv M_{\text{eff}}^{\text{light}} - M_{\text{eff}}^{\text{dark}}$ is 47 mT at 300 K with 4.66 $\text{mW}\cdot\text{cm}^{-2}$ low-intensity white light illumination in an $MAPbI_3$/LSMO sample of T_C = 360 K. This is equivalent to about 7% change of $\Delta M_{\text{eff}}/M_{\text{eff}}$. Conversely, the same stimulus for an $MAPbI_3$/LSMO sample with T_C = 310 K results in $\Delta M_{\text{eff}} = 32$ mT, which is over 30% change. We suggest that this strong decrease in magnetization and its tunability allow an easy and rapid rewriting of the magnetic bit at room temperatures.

Results and Discussions

LSMO is a well-known correlated oxide, which shows ferromagnetism above room temperature. Its T_C is tunable by the carrier concentration (Fig. 1*A*) (1) and by the thickness of the thin film (22). Here, three thin films (denoted by points S1 to S3 in Fig. 1*A*) were selected, with T_C = 360 K (film thickness: 29 nm), 310 K (14 nm), and 210 K (11 nm), on the $SrTiO_3$ substrate and coated with $MAPbI_3$ (see Fig. 1*B* and *Materials and Methods* for synthesis details) (23, 24). Upon illumination, photoelectron transfer is induced from $MAPbI_3$ to LSMO (Fig. 1 *C* and *D*). The resulting photodoping reduces the magnetization of the film. We used electric resistivity, magnetic inductance, and ferromagnetic resonance (FMR) spectroscopy to monitor the light-induced changes in the electronic and magnetic properties of LSMO. The experimental setups are depicted in Fig. 2 *A* and *D* for magnetic inductance and FMR, respectively.

Our major finding is that the magnetization, ΔM, of the LSMO thin film of the $MAPbI_3$/LSMO heterostructure can be tuned above room temperature by visible light illumination, as shown in Fig. 2. To measure M, the change of the remnant magnetization induced by the change of the incident light intensity, we designed a setup to take advantage of Faraday's law and pick up the induced voltage, $V_{\text{ind}}(t)\ \text{d}M/\text{d}t$, in a coil. A 30-mW (about 3 to 4 $\text{mW}\cdot\text{cm}^{-2}$) 660-nm-wavelength light was periodically switched on and off at a frequency f. The amplitude of the induced AC voltage (V_{ind}) in the coil was measured by a lock-in amplifier, shown in Fig. 2 *A–C* (see *Materials and Methods* for more details). V_{ind} was found to be proportional to f as expected from Faraday's law (Fig. 2*C*). This light-induced magnetization change is attributed to the $MAPbI_3$ layer, which acts as a photosensitizer that injects photoinduced electrons into the LSMO film due to the mismatch of the chemical potentials (Fig. 1 *C* and *D*).

Acquired from various electric characterizations of the $MAPbI_3$/LSMO interface, the scenario based on photoinduced electron injection from $MAPbI_3$ to LSMO is reinforced. The intrinsic timescale of the light-induced magnetization change is fast. It is far beyond our 100-kHz (10 μs) experimental limit of the Faraday experiment (Fig. 2 *A–C*). We observed the change in the magnetization with 660-nm light pulses as short as 6.25 ns (80-MHz repetition rate with a high-frequency lock-in; see *Materials and Methods* for more details). These indicate that the light-induced change at the interface is electronic in origin.

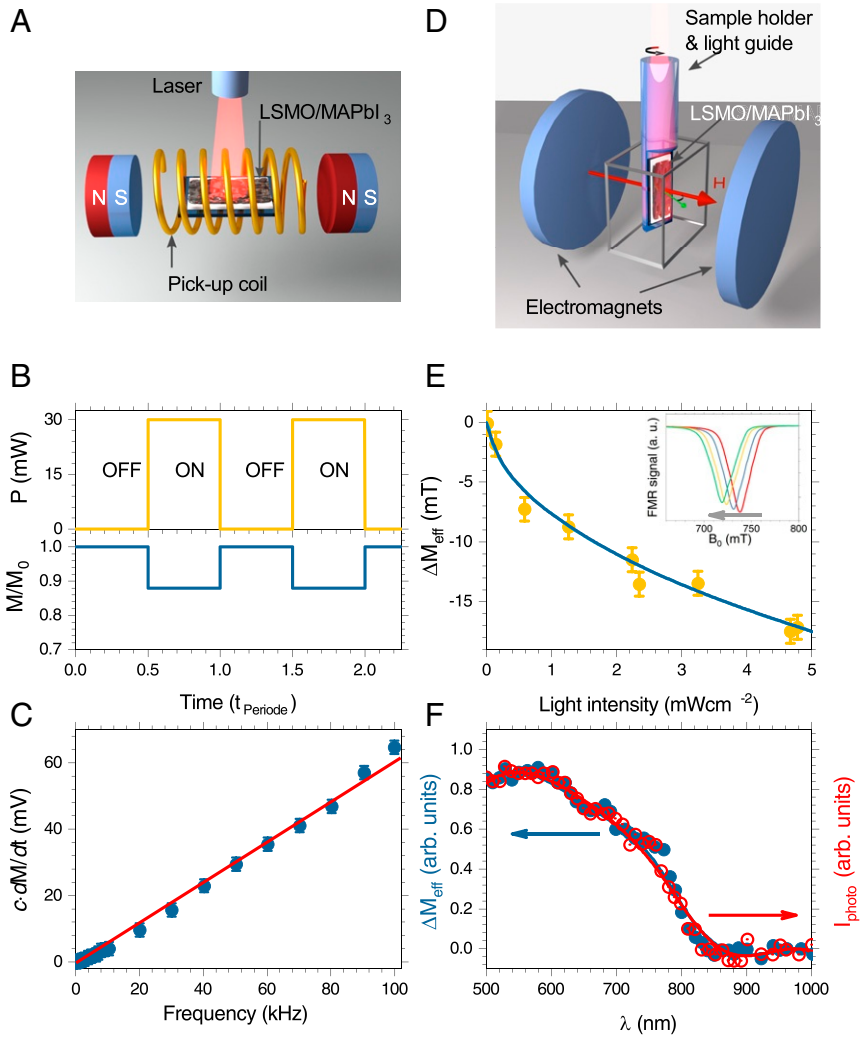

Fig. 2. Visible light control of $MAPbI_3$/LSMO heterostructures at 300 K. For the experiments, the sample denoted by S2 in Fig. 1 was used. (*A*) Schematic drawing of the setup to pick up the induced voltage, $V_{ind} \propto dM/dt$, according to Faraday's law; (*B*) the time sequence of the illumination (upper part) and the resulting response in magnetization (lower part), and (*C*) the frequency dependence of the induced voltage dM/dt obtained in the Faraday experiment. (*D*) Sketch of the FMR experiment with the sample holder of the heterostructure mounted in the center of the 9.4-GHz microwave cavity. The polar angle of the magnetic field H is varied by rotation of the sample holder. (*E*) Visible light tuning of the effective magnetization M_{eff} at 300 K. The continuous line is a fit to $M^0_{eff} - (a \cdot I + (b \cdot I)^{0.5})$ function, where I is the light intensity, $a = 0.14$ mT·mW^{-1}·cm^2, and $b = 78.85$ mT^2·mW^{-1}·cm^2. This functional form is expected to come from photodoping as explained in the main text. (*Inset*) FMR spectra of $MAPbI_3$/LSMO perovskite heterostructure as a function of the illuminating white light intensity. The intensity of white light was 0, 0.033, 0.586, 2.33, and 4.66 mW·cm^{-2}; the arrow points toward increasing light intensities. The magnetic field was applied perpendicular to the interface. The shift of the FMR line is the consequence of photodoping-induced suppression of magnetic order of LSMO. (*F*) Photoinduced change of the effective magnetization M_{eff} (left scale) and photocurrent I_{photo} (right scale) as a function of the incident light wavelength, showing that magnetization change sets in with photon energies beyond the band gap of $MAPbI_3$. For the experiments, the sample denoted by S2 in Fig. 1 was used.

To further characterize the built-in electrostatic potential at the $MAPbI_3$/LSMO interface, we studied the high-quality photodiode response of the structure (*SI Appendix*, Fig. S1). Illuminating the heterostructure with 10 mW·cm^{-2} 660-nm intensity light, the diode current increases by about three orders of magnitude at a drain-source voltage (V_D) of 20 V. Similar photosensitizer behavior of $MAPbI_3$ associated with different substrates like graphene and carbon nanotubes was already reported (25–27). The combined electric and magnetic tunability of the heterostructure's response indicates that photodoping takes place at the $MAPbI_3$/LSMO interface where an electrostatic barrier, Φ_B, is formed. The sketch of the energy band structure is shown in Fig. 1 *C* and *D*. White light illumination excites holes from the valence band of $MAPbI_3$ to its conduction band. As a consequence, holes from LSMO diffuse to $MAPbI_3$ while photoexcited electrons diffuse to the LSMO. This changes Φ_B and also alters the carrier density of LSMO (Fig. 1*D*). The change of Φ_B upon illumination results in a 60-fold increase of thermionic emission, and a decrease of 54% for the ideality factor of the diode formed at the $MAPbI_3$/LSMO interface (see *Materials and Methods* and *SI Appendix*, Fig. S1 for more details). The photodoping of LSMO by light-induced carriers of $MAPbI_3$ grants functionalities to the $MAPbI_3$/LSMO heterostructure, because the electronic state of LSMO is highly sensitive to carrier concentration (see phase diagram in Fig. 1*A*).

The chemical effects can be excluded, since both the electronic and magnetic responses to illumination were absent on pristine films of LSMO (*SI Appendix*, Figs. S1 and S2). We extensively looked for possible chemical modifications such as redox reactions, ion exchange, and photocorrosion

of the surface of the LSMO films during the growth of $MAPbI_3$ by energy-dispersive X-ray (EDX) spectroscopy, and they were absent (*SI Appendix*, Fig. S3). Furthermore, the repeatability of the $MAPbI_3$ growth and removal on the very same LSMO substrate resulted in similar experimental observations of modulation of magnetization upon illumination by visible light. Specifically, repeatability of the process can exclude oxygen deficiency as the source of suppression of ferromagnetism. We also fabricated heterostructures of LSMO and the Cl and Br variants of methylammonium lead halide perovskites using the same LSMO film, and preliminary data show similar light-tunable magnetism (*SI Appendix*, Fig. S4). This is a clear proof of the absence of any local chemical effect such as modification of chemical doping of LSMO or a new alloy formation at the interface.

To distinguish photodoping from heating effects (28, 29), we used FMR (Fig. 2*D*), which is a sensitive and frequently applied probe for magnetization, magnetic anisotropies, and spin dynamics of ferromagnetic thin films. M_{eff}, directly obtainable from FMR compared to the paramagnetic resonance position of about 330 mT (see *Materials and Methods* for more details), is the parameter that characterizes the stability of the magnetization of the magnetic domain in a given external magnetic field. It is a combination of static magnetization and shape and magnetocrystalline anisotropies. The fitted $M_{\text{eff}}^0 - (a \cdot I - \sqrt{b \cdot I})$ light intensity dependence of M_{eff}, where I is the light intensity and a and b are constants (Fig. 2*E*), is clear evidence of the photodoping scenario. The number of photocarriers in methylammonium lead iodide nanowires also follows this dependence as a function of light intensity (30). Thus, a linear dependence of ΔM_{eff} of LSMO on carrier concentration describes the experimental points remarkably well (full line in Fig. 2*E*).

The wavelength dependence of both ΔM_{eff} and photocurrent I_{ph} (Fig. 2*F*) also demonstrates that the photoinduced electrons are injected from the hybrid organic–inorganic perovskite layer and change the magnetization of LSMO: I_{ph} sharply drops at the band edge of $MAPbI_3$ of about 780 nm (1.5 eV). This trend is closely followed by ΔM_{eff} of LSMO.

The ferromagnetic metallic state of LSMO is very sensitive to external stimuli in the vicinity of T_C. That is the temperature range where the CMR is also the most pronounced (31). As further proof for photodoping-induced fine-tuning of T_C, we studied electronic transport properties of the heterostructure with T_C = 310 K (S2 in Fig. 1), because this film allows reaching temperatures well above its T_C conveniently. We found that the light effect is the largest slightly below T_C, in perfect agreement with the proposed photodoping-driven modulation of T_C. To further characterize the light-induced magnetic change of the $MAPbI_3$/LSMO heterostructure, the temperature dependence of the magnetization and CMR with and without light illumination were studied.

The effective magnetizations, M_{eff}, in the dark and under 4.66 $\text{mW}\cdot\text{cm}^{-2}$ white light illumination are compared in Fig. 3. They differ significantly in the 270- to 310-K temperature range, slightly below T_C. The difference, ΔM_{eff}, peaks at around 288 K. The maximum light-induced change in magnetization, $\Delta M_{\text{eff}}/M_{\text{eff}}$, is over 30% for this light intensity at room temperature (*SI Appendix*, Figs. S5 and S6), but it can be freely tuned by the appropriate choice of temperature and light intensity. The temperature dependence corresponds to a 6.5 K decrease of T_C upon illumination (Fig. 3). The observed shift of T_C in Fig. 3 would correspond to 0.5% effective change in Sr concentration, equivalent to $7\cdot10^{19}$ cm^{-3} decrease of the carrier concentration, n, of LSMO, assuming that T_C linearly changes with the n in the vicinity of the composition $La_{0.7}Sr_{0.3}MnO_3$. The observed photoinduced change in the doping level is equivalent to 0.1-V electrolyte gating of similar LSMO films (9).

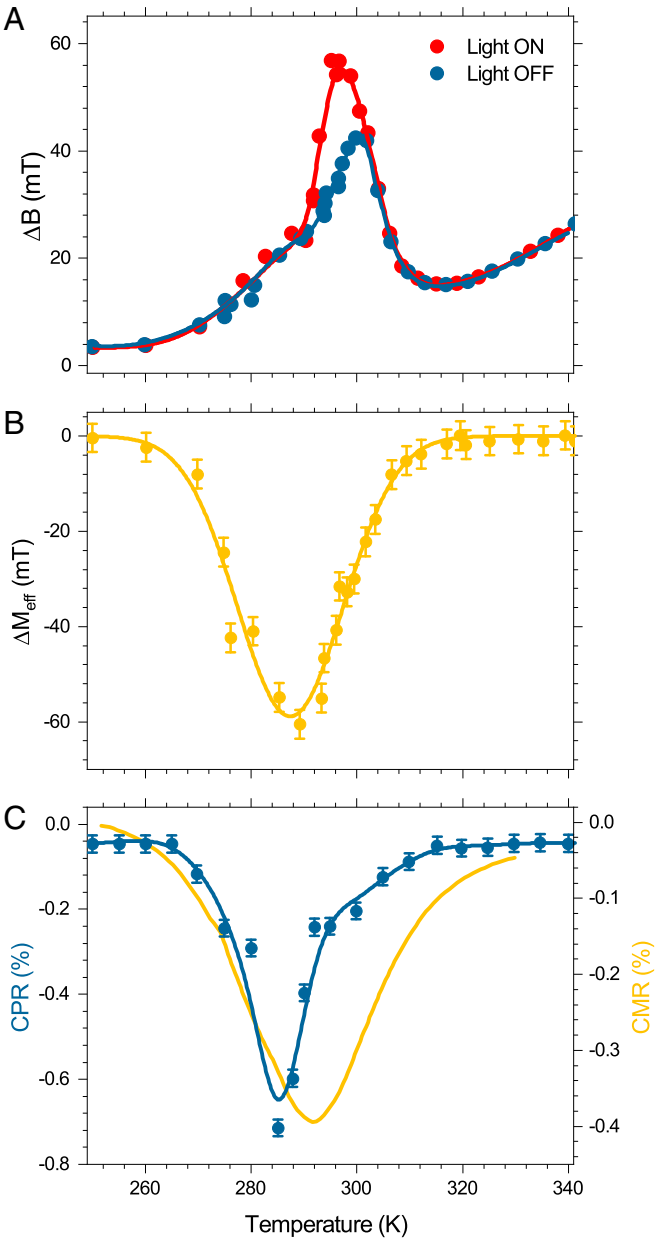

Fig. 3. Temperature-dependent photoresponse of $MAPbI_3$/LSMO perovskite heterostructures in the 250- to 350-K range. (*A*) Temperature dependence of the FMR linewidth ΔB in the dark and under 4.66 $\text{mW}\cdot\text{cm}^{-2}$ white light illumination (blue and red, respectively). The peaks around 300 K in the dark and at 295 K under illumination are due to slowing down of critical fluctuations, and signal the ferromagnetic phase transition (21, 22). The increased linewidth in the illuminated state shows that the change of magnetization is due to photodoping and cannot be caused by any thermal effect. (*B*) Temperature dependence of photodoping-induced magnetization change of LSMO, ΔM_{eff}. A Gaussian line to guide the eye is centered at $T = 288$ K with a maximum change of 61 mT or 26% of M_{eff}. This Gaussian fit of the magnetization change approximates well the difference of the temperature dependence of the two spontaneous magnetization curves. (*C*) CPR = $(R_{\text{dark}} - R_{\text{light}})/R_{\text{dark}}$ peaks sharply with 0.8% value below T_C (blue points; the line is a guide to the eye). The yellow line is a CMR = $(R_{B=0\text{T}} - R_{B=1.5\text{T}})/R_{B=0\text{T}}$ signal measured with a 1.5-T magnetic field applied normal to the film. Note that the photoinduced CPR is the resistivity change between samples with different T_C, whereas the field-induced CMR is the result of a decrease of localization in a system with a given T_C. The different origins result in maxima at slightly different temperatures. For the experiments, the LSMO film denoted as S2 (Fig. 1*A*) was used.

At low temperatures, M_{eff} is the same for light-on and light-off conditions (*SI Appendix*, Fig. S5), which indicates that neither the saturation magnetization nor the 0-K magnetic anisotropy is influenced by light. The light-induced effect is indeed due to a decrease of T_{C} by photodoping in the vicinity of the metal–insulator transition, as depicted in Fig. 1*D*.

It is crucial to exclude local heating as the origin of the observed effect. Normally, this would not be easy to discard. Here, however, we can take advantage of the rich information provided by FMR, as local temperature increase due to illumination would change, simultaneously, both the position (M_{eff}) and the linewidth (ΔB) of the resonance (28). As detailed in Fig. 3*A*, maximal ΔB under light (at 288 K) reaches a value almost two times larger than the maximal ΔB in the dark. In the case of local heating, light-on and light-off curves of $\Delta B(T)$ (and $\Delta M_{\mathrm{eff}}(T)$) could be superimposed by simply shifting temperature, which is not possible for these differing values (see further details in *SI Appendix*, Fig. S7). Instead, photoexcited electrons of the photovoltaic perovskite injected into LSMO destabilize the ferromagnetic order and provide a handle on ferromagnetism. The short timescale of the magnetization decrease below about 6 ns of our experimental resolution further supports this scenario.

It is natural to expect that photodoping and the consequent change of carrier concentration show up in the electronic transport properties of the LSMO film, as well. Indeed, the resistivity of the LSMO film drops upon 4.66 $\mathrm{mW{\cdot}cm^{-2}}$ white light illumination. This change in resistivity is comparable to the effect of about 0.2-V gating of similar LSMO films (9). This gating level is in perfect agreement with the expected modification in the band structure. Moreover, colossal photoresistance (CPR), the light-induced analogy of the magnetic field-induced CMR, was observed in the vicinity of T_{C} (Fig. 3*C*). The CPR signal for 4.66 $\mathrm{mW{\cdot}cm^{-2}}$ white light illumination is 0.8%, which is equivalent to a CMR signal for 30-mT magnetic field.

It is interesting to note that there is a slight shift in the peak temperature in CMR and CPR, found at 286 and 295 K, respectively. We believe that this temperature difference comes from the different microscopic origins of the resistance decrease. In the former case, the magnetic field polarizes the spin orientations, promoting better conduction by the double exchange mechanism. It is most effective in the vicinity of the insulator–metal transition, where the spins on the $\mathrm{Mn^{3+}}$ are still fluctuating. In the case of photodoping, CPR [or doping with ionic liquid (9)], the effect is the largest when the system is "almost" metallic when an additional charge can improve the conduction significantly. However, T_{C} is reduced by photodoping. Thus, the CPR maximum is expected at lower temperatures than the CMR maximum, found at the range where magnetic fluctuations are strong enough.

We demonstrated that the maximum of CPR could be tuned to a given temperature in the present LSMO/$\mathrm{MAPbI_3}$ heterostructure by choosing T_{C} of LSMO, by adjusting the Sr concentration of the thin film. In Fig. 4, LSMO/$\mathrm{MAPbI_3}$ heterostructures with T_{C} = 360, 310, and 210 K were illuminated by 4.66 $\mathrm{mW{\cdot}cm^{-2}}$ white light, and the strongest decrease in ΔM_{eff} is observed a few degrees below T_{C}. This is a clear demonstration that the "operating temperature" is easily tunable in the 145- to 371-K range by the appropriate choice of Sr concentration and postsynthesis heat treatment (Fig. 4) (32).

The observed photodoping and the resulting change of magnetic properties could go beyond basic science, and it could be of practical importance, especially due to the tunability of ΔM_{eff} (and $\Delta M_{\mathrm{eff}}/M_{\mathrm{eff}}$) and T_{C}. Consider, as an example, a magnetic thin film of a hard drive. By using simple patternability of the $\mathrm{MAPbI_3}$ layer (27), small magnetic bits could be defined. In the presence of illumination, writing could be achieved with a significantly weaker magnetic field than the one needed in existing technologies, rendering data storage faster and allowing smaller bits. Its principle (sketched in *SI Appendix*, Fig. S9) is conceptually similar to the long-time proposed heat-assisted magnetic recording (HAMR) but offers several advantages. Photodoping and the subsequent magnetization change is an electronic phenomenon, so it is very likely that it is taking place within characteristic timescales of electron–electron interactions, in the range of femtoseconds to picoseconds (28, 33). Moreover, it is unrelated to heating; thus thermal stress, materials' fatigue, and even read–write time limitations due to heat transport do not play a role. These improvements could overcome the difficulties that have prevented commercial implementation of HAMR for over 10 y, despite numerous propositions (34).

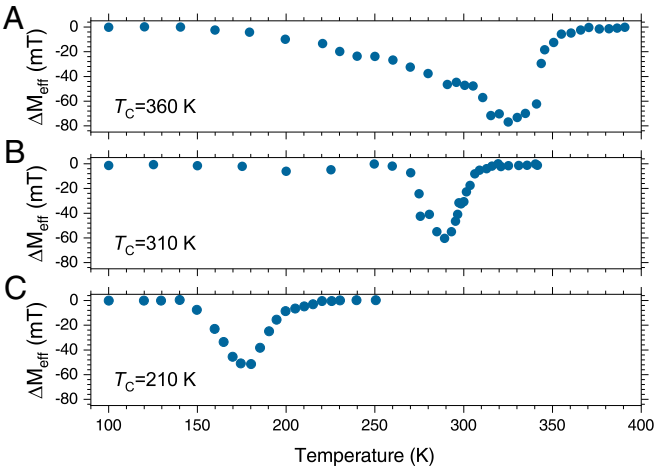

Fig. 4. Tuning magnetism by decreasing the T_{C} of LSMO: Temperature dependence of ΔM_{eff} induced by 4.66 $\mathrm{mW{\cdot}cm^{-2}}$ white light illumination of LSMO/$\mathrm{MAPbI_3}$ heterostructures with T_{C} = 360, 310, and 210 K denoted by S1, S2, and S3, respectively, in Fig. 1.

In summary, we observed a strong photoinduced doping effect in halide perovskite/oxide perovskite heterostructures and provided a microscopic description of its origin. This technique enables disorder-free exploration of the phase diagram of strongly correlated electron systems. Moreover, it allows repeatable crossing of the magnetic transition in LSMO without changing the temperature. This simple technique in writing magnetic bits opens the door to scientific studies and applications.

Materials and Methods

$\mathrm{La_{0.7}Sr_{0.3}MnO_3}$ Thin Films. $\mathrm{La_{0.7}Sr_{0.3}MnO_3}$ thin films were grown on (100) $\mathrm{SrTiO_3}$ single-crystal substrates using magnetron sputtering, in 0.06-mbar flowing Argon pressure. The substrate was at room temperature during sputtering and was then annealed after film growth in flowing oxygen at 800 °C for an hour. For each sample, the film thickness was determined from X-ray reflectometry. The thicknesses of the samples are as follow: S1 is 29 nm, S2 is 14 nm, and S3 is 11 nm.

$\mathrm{CH_3NH_3PbI_3}$ Nanowire Coatings. $\mathrm{CH_3NH_3PbI_3}$ nanowire coatings were prepared by the slip-coating method. Methylammonium lead iodide was prepared by precipitation from a concentrated aqueous solution of hydriodic acid (57 wt % in $\mathrm{H_2O}$, 99.99%; Sigma-Aldrich) containing lead (II) acetate trihydrate (99.999%; Acros Organics), and a respective amount of $\mathrm{CH_3NH_2}$ solution (40 wt% in $\mathrm{H_2O}$; Sigma-Aldrich). A constant 55 °C to 42 °C temperature gradient was applied to induce saturation of the solute at the low-temperature part of the solution (23). Besides the formation of hundreds of submillimeter-sized crystallites, several large $\mathrm{MAPbI_3}$ crystals with 3 × 5 mm silver-gray mirror-like facets were grown after 21 d. The as-prepared polycrystalline powder was dissolved in dimethylformamide (DMF; Sigma-Aldrich). One microliter of a saturated solution (~50 wt %) of $\mathrm{MAPbI_3}$ in DMF was dropped onto an LSMO substrate and covered with a microscope slide so that the excess yellow solution squeezed out; the remaining solution formed a homogenous liquid film between the glass plates. The excess of the $\mathrm{MAPbI_3}$ solution was removed from the sides by soaking

with a tissue. Next, the bottom substrate was held in place while gradually sliding the upper glass plate, exposing the thin liquid film to air. Solvent evaporation from the uncovered surface caused an instantaneous formation of a white-yellow solvatomorph $MAPbI_3$ (DMF) nanowire coating. Subsequent heat treatment at 80 °C to 100 °C results in the nearly instantaneous appearance of a brown-red to gray color, indicating the crystallization of $MAPbI_3$ nanowire coating. The thickness of the coating was in the range of several microns, below the diffusion length of $MAPbI_3$ (33, 35).

$CH_3NH_3PbBr_3$ Coatings. Crystals of methylammonium lead tribromide were synthesized by solution growth. A 3.3-mmol sample of lead(II) acetate trihydrate ($Pb(ac)_2 \cdot 3H_2O$, >99.9%) was reacted with 6 mL of saturated HBr solution (48 wt % HBr in H_2O). The formed $PbBr_2$ precipitate is stable in the acidic solution. The respective amount (3.30 mmol) of methylamine (CH_3NH_2) solution (40 wt % in H_2O) was pipetted into the 5 °C ice-cooled solution of $PbBr_2$. The cold solution avoids the evaporation of methylamine during the exothermic reaction. Orange colored microcrystallites of $CH_3NH_3PbBr_3$ were formed. The $MAPbBr_3$ crystals were recrystallized in a temperature gradient of 15 °C in the acidic media to get high purity crystals. The as-prepared crystals were dissolved in DMF (Sigma-Aldrich). One microliter of a saturated solution (~30 wt %) of $MAPbBr_3$ in DMF was dropped onto an LSMO substrate and covered with a microscope slide so that the excess orange solution squeezed out; the remaining solution formed a homogenous liquid film between the flat surfaces. The excess of the $MAPbBr_3$ solution was removed from the sides by soaking with a tissue. Next, the bottom substrate (LSMO) was heated to 80 °C, held in place while gradually sliding the upper glass plate, exposing the thin liquid film to air. Solvent evaporation from the uncovered surface caused an instantaneous formation of an orange $MAPbBr_3$ coating composed of cube-like crystallites.

$CH_3NH_3PbCl_3$ Coatings. The $CH_3NH_3PbCl_3$ crystals were synthesized by solution growth, using the same molar amounts and receipt as for the $MAPbBr_3$ synthesis, but using HCl (36 wt % in H_2O) reagent instead of the HBr solution. The $MAPbCl_3$ solution was prepared by dissolving the as-prepared single crystals in 1:1 DMF:dimethyl sulfoxide solvent mixture. The coatings on LSMO films were prepared in a fashion similar to the $MAPbBr_3$ solution. Cube-shaped crystallites were grown on the LSMO surface.

$La_{0.7}Sr_{0.3}MnO_3/CH_3NH_3PbI_3$ Nanowire Heterostructure Preparation. $La_{0.7}Sr_{0.3}MnO_3/CH_3NH_3PbI_3$ nanowire heterostructure preparation was repeated several times on the very same LSMO substrate. The cleaning procedure involved placing the heterostructure in DMF and sonicating in an ultrasonication bath for 10 min. The ultrasound-assisted cleaning procedure was then repeated in acetone and isopropanol solvents, as well. The LSMO film was dried with an argon air gun, and the $CH_3NH_3PbI_3$ nanowire coating was grown by the slip-coating method described above.

Scanning Electron Microscopy. Scanning electron microscope images were taken with a Zeiss (LEO) electron microscope. Aluminum pucks were used for sample support. Conducting carbon tape served as an electric contact between the sample and the support.

Energy-Dispersive X-ray Spectroscopy. The elemental composition of the $MAPbI_3$ crystallites was analyzed by EDX (accelerating voltage of 8 kV, the working distance of 8.5 mm). Samples were mounted on Al pucks with carbon tape with electrical contact to the surface also formed by carbon tape. The measurement was performed with an X-Max energy-dispersive X-ray spectroscopy (EDS) detector mounted at a 35° takeoff angle with a super atmospheric thin window (SATW). EDS spectra were obtained at a working distance of 8.5 mm with 8-keV accelerating voltage and a current held at 184 pA; 2,048 channels were used for the acquisitions, corresponding to the energy of 5 eV per channel. Spectra were acquired over 1,573 s of live time, with detector dead time averaging of 4% and a dwell time per pixel of 500 μs. Quantitative EDS analysis utilized Aztec software provided by Oxford Instrument Ltd.

Electronic Characterization of $MAPbI_3$/LSMO. Electronic characterization of $MAPbI_3$/LSMO was performed in a two- and four-terminal method. For electrical contacts, 50-μm gold wires were glued onto the LSMO surface using silver paste. Contacts were electronically isolated by STYCAST 2850FT epoxy before thin films of $MAPbI_3$ were precipitated on top of the LSMO. Resistances were measured in two- and four-point configurations. The former one gives a factor of 2 higher resistance than the latter but essentially the same dependence on temperature or illumination. Resistivity was calculated using an effective thickness of 16 nm, the thickness of the LSMO film. Resistivity was recorded as a function of the magnetic field and light intensity in the 5- to 330-K temperature range. Magnetotransport experiments up to 1.5 T were performed in a magnetic field perpendicular to the [001] direction of LSMO. The light of a halogen lamp was guided to the sample through a quartz sample holder rod with switchable light intensity. The experimental setup is depicted in Fig. 2.

Zero-Field Magnetic Photoresponse. Zero-field magnetic photoresponse based on Faraday's law was observed in a setup consisting of a homemade copper-wound coil set (solenoid) that allowed illumination of the sample. The coil was positioned between two small NdFeB magnets to place the sample in a small bias field of 23 mT so that magnetization would be oriented in a definite direction, and to prevent a possible multidomain state. The sample was placed at the center of the coil set and illuminated with 660-nm 30-mW light (Arima Lasers ADL66505TL). Light intensity was periodically turned off at a given frequency, f, between 1 kHz and 102 kHz—the upper limit of the employed SR830 lock-in amplifier. The average intensity (modulation included) was measured by a photodiode for each frequency, to eliminate any possible electronic drift in driving the laser. The open-circuit voltage of the coil set was recorded at the light modulation frequency with the lock-in amplifier. This voltage is proportional to the magnetic flux changes in the coil set, and to the modulation frequency, as given by Faraday's law, $V_{ind} = C_{geom} \cdot f \cdot M_{rem}$, where C_{geom} is a geometric proportionality factor relating the flux created by the sample in the coil set and its remanent magnetization.

As a control experiment, we measured an uncoated LSMO film in the same setup where we did not observe any photoresponse in the lock-in amplifier down to 5 nV with a long, 10-s time constant.

In order to estimate the timescale of the light-induced decrease of magnetization, we performed experiments with 6.25-ns light pulse width provided by an Arima Lasers ADL66505TL diode directly powered by an Agilent 33250A Function/Arbitrary Waveform Generator, while the magnetization change was detected by a high-frequency SR844 lock-in amplifier. The magnetization was clearly altered by this short (about 6 ns) light pulse, but our setup does not allow detailed frequency-dependent measurements.

Interestingly, this method of observing the magnetic moment of a sample is inspired by commercial vibrating sample magnetometers, where the static magnetic moment of a sample is turned into a changing flux by moving (vibrating) the sample back and forth along the coils axis. Here, we can dispense with such movement, since it is the photoresponse of the LSMO/$MAPbI_3$ that provides the modulation of the flux.

FMR. FMR was performed using a commercial 9.4-GHz Bruker Electron Spin Resonance spectrometer. For temperature-dependent experiments, below 300 K, a He-flow cryostat was used. We used an N_2-flow cryostat for experiments between 250 K and 350 K temperature. We analyzed the FMR assuming out-of-plane and fourfold in-plane anisotropy: $K_\perp$ and K_4, respectively. These are effective anisotropy constants resulting from both bulk and surface energy terms. The free energy density E is written as

$$E = -M_S H[\sin\theta_M \sin\theta_H \cos(\Phi_M - \Phi_H) + \cos\theta_M \cos\theta_H] - (2\pi M_S - K_\perp)\sin^2\theta_M - \frac{1}{8}K_4[3 + \cos^4(\Phi_M - \Phi_H)]\sin^4\theta_M,$$

where M_S is the magnetization at saturation. The angles θ_M, θ_H, Φ_M, and Φ_H are depicted in *SI Appendix*, Fig. S8, which shows the coordinate system. The FMR frequency F is obtained from E as (29)

$$F^2 = \left(\frac{g\mu_B}{2\pi}\right)^2 \frac{1}{M_S^2 \sin^2\theta_M}\left[\frac{\partial^2 E}{\partial^2\theta_M}\frac{\partial^2 E}{\partial^2\Phi_M} - \left(\frac{\partial^2 E}{\partial\theta_M \partial\Phi_M}\right)^2\right], \quad [1]$$

where g is the Lande factor, μ_B is the Bohr magneton, and the derivatives are evaluated at the equilibrium position.

Internal Electric Field Characterization. The current through the Schottky diode formed by $MAPbX_3$ (X = Cl, Br, or I) and LSMO, I_{diode}, is analyzed in the frame of the thermionic emission diffusion equation (36)

$$I_{diode} = I_S\left(\exp\left[\frac{q(V - I_{diode}R_S)}{\eta k_B T}\right] - 1\right), \quad [2]$$

where I_S is the thermionic emission, T is the diode temperature, q is the electronic charge, k_B is the Boltzmann constant, V is the applied bias, η is the ideality factor, and R_S is the diode series resistance.

The experimental setup and results for LSMO film S1 are depicted in *SI Appendix*, Fig. S1. A Keithley 2400 Source Meter was used to bias the diode and to monitor the diode current.

In the model, there are two free parameters: I_S and η, the thermionic emission and ideality factor, respectively. The least-square fit of the model to the data yields

$$\begin{array}{rcl} I_S^{\text{light}} = & 0.036 \pm 0.005 & (15.2\%) \\ \eta^{\text{light}} = & 1.8 \pm 0.1 & (5.7\%) \\ I_S^{\text{dark}} = & (5.6 \pm 0.7) \cdot 10^{-4} & (12.4\%) \\ \eta^{\text{dark}} = & 3.27 \pm 0.24 & (7.4\%) \end{array}. \quad [3]$$

Accordingly, the mentioned 60-fold increase of thermionic emission is $I_S^{\text{light}}/I_S^{\text{dark}} = 63 \pm 17$, while $\eta^{\text{light}}/\eta^{\text{dark}} = 0.54 \pm 0.07$ is the 54% reduction of the ideality factor.

Photocurrent Spectroscopy. The monochromatic light was selected from the output of a 75-W Xeon arc lamp (PTI PowerArc) by a Horiba MicroHR imaging Monochromator. The setup has output above 180 nm with 10-nm wavelength resolution and 0.1-mW intensity. The photocurrent was monitored by cavity perturbation method implemented in the X-band electron spin resonance spectrometer's cavity. The light intensity was periodically chopped by a turning blade, and the change in Q factor far from resonance was detected by a lock-in amplifier. The magnetization change as a function of light wavelength was measured by the same setup, but the magnetic field was tuned to the maximum of the FMR absorption.

Data Availability. All of the scripts and all of the experimental data used to produce the figures within this work are available at https://doi.org/10.5281/zenodo.3662206.

ACKNOWLEDGMENTS. The work in Lausanne was supported by the Swiss National Science Foundation (Grant 200021 144419) and European Research Council (ERC) advanced grant "Photo Induced Collective Properties of Hybrid Halide Perovskites" ("PICOPROP") (Grant 670918). The work in Madrid was supported by Spanish Ministry of Economy and Competitiveness (MINECO) Grant MAT2014-52405-C02-02 and by Spanish Ministry of Science, Innovation and Universities (MICIIN) project MAT2017-84496-R.

1. J. Hemberger *et al.*, Structural, magnetic, and electrical properties of single-crystalline $La_{1-x}Sr_xMnO_3$ ($0.4<x<0.85$). *Phys. Rev. B* **66**, 094410 (2002).
2. M. B. Salamon, M. Jaime, The physics of manganites: Structure and transport. *Rev. Mod. Phys.* **73**, 583–628 (2001).
3. S. Jin *et al.*, Thousandfold change in resistivity in magnetoresistive La-Ca-Mn-O films. *Science* **264**, 413–415 (1994).
4. A. Ohtomo, H. Y. Hwang, A high-mobility electron gas at the $LaAlO_3/SrTiO_3$ heterointerface. *Nature* **427**, 423–426 (2004).
5. N. Reyren *et al.*, Superconducting interfaces between insulating oxides. *Science* **317**, 1196–1199 (2007).
6. A. Brinkman *et al.*, Magnetic effects at the interface between non-magnetic oxides. *Nat. Mater.* **6**, 493–496 (2007).
7. W. Eerenstein, M. Wiora, J. L. Prieto, J. F. Scott, N. D. Mathur, Giant sharp and persistent converse magnetoelectric effects in multiferroic epitaxial heterostructures. *Nat. Mater.* **6**, 348–351 (2007).
8. I. Fina *et al.*, In-plane tunnelling field-effect transistor integrated on silicon. *Sci. Rep.* **5**, 14367 (2015).
9. B. Cui *et al.*, Reversible ferromagnetic phase transition in electrode-gated manganites. *Adv. Funct. Mater.* **24**, 7233–7240 (2014).
10. H. T. Yi, B. Gao, W. Xie, S. W. Cheong, V. Podzorov, Tuning the metal-insulator crossover and magnetism in $SrRuO_3$ by ionic gating. *Sci. Rep.* **4**, 6604 (2014).
11. A. S. Dhoot, C. Israel, X. Moya, N. D. Mathur, R. H. Friend, Large electric field effect in electrolyte-gated manganites. *Phys. Rev. Lett.* **102**, 136402 (2009).
12. S. M. Wu *et al.*, Reversible electric control of exchange bias in a multiferroic field-effect device. *Nat. Mater.* **9**, 756–761 (2010).
13. A. Alekhin *et al.*, Femtosecond spin current pulses generated by the nonthermal spin-dependent Seebeck effect and interacting with ferromagnets in spin valves. *Phys. Rev. Lett.* **119**, 017202 (2017).
14. M. Först *et al.*, Spatially resolved ultrafast magnetic dynamics initiated at a complex oxide heterointerface. *Nat. Mater.* **14**, 883–888 (2015).
15. A. V. Kimel, A. Kirilyuk, A. Tsvetkov, R. V. Pisarev, T. Rasing, Laser-induced ultrafast spin reorientation in the antiferromagnet $TmFeO_3$. *Nature* **429**, 850–853 (2004).
16. C. Stamm *et al.*, Femtosecond modification of electron localization and transfer of angular momentum in nickel. *Nat. Mater.* **6**, 740–743 (2007).
17. R. Cauro *et al.*, Persistent and transient photoconductivity in oxygen-deficient $La_{2/3}Sr_{1/3}MnO_{3-\delta}$ thin films. *Phys. Rev. B* **63**, 174423 (2001).
18. Z. G. Sheng, Y. P. Sun, J. M. Dai, X. B. Zhu, W. H. Song, Erasure of photoconductivity by magnetic field in oxygen-deficient $La_{2/3}$ $Sr_{1/3}MnO_{3-\delta}$ thin films. *Appl. Phys. Lett.* **89**, 082503 (2006).
19. G. Nieva *et al.*, Photoinduced enhancement of superconductivity. *Appl. Phys. Lett.* **60**, 2159–2161 (1992).
20. V. Peña, T. Gredig, J. Santamaria, I. K. Schuller, Interfacially controlled transient photoinduced superconductivity. *Phys. Rev. Lett.* **97**, 177005 (2006).
21. M. Dumm *et al.*, Comprehensive ESR study of the antiferromagnetic ground states in the one-dimensional spin systems $(TMTSF)_2PF_6$,$(TMTSF)_2AsF_6$, and $(TMTTF)_2Br$. *Phys. Rev. B* **62**, 6512–6520 (2000).
22. Å. Monsen *et al.*, Thickness dependence of dynamic and static magnetic properties of pulsed laser deposited $La_{0.7}Sr_{0.3}MnO_3$ films on $SrTiO_3$ (001). *J. Magn. Magn Mater.* **369**, 197–204 (2014).
23. E. Horváth *et al.*, Nanowires of methylammonium lead iodide ($CH_3NH_3PbI_3$) prepared by low temperature solution-mediated crystallization. *Nano Lett.*. **14**, 6761–6766 (2014).
24. F. Y. Bruno *et al.*, Electronic and magnetic reconstructions in $La_{0.7}Sr_{0.3}MnO_3/SrTiO_3$ heterostructures: A case of enhanced interlayer coupling controlled by the interface. *Phys. Rev. Lett.* **106**, 147205 (2011).
25. P. Zhao *et al.*, Calcium manganate: A promising candidate as buffer layer for hybrid halide perovskite photovoltaic-thermoelectric systems. *J. Appl. Phys.* **116**, 194901 (2014).
26. M. Spina *et al.*, Microengineered $CH_3NH_3PbI_3$ nanowire/graphene phototransistor for low-intensity light detection at room temperature. *Small* **11**, 4824–4828 (2015).
27. M. Spina *et al.*, Controlled growth of $CH_3NH_3PbI_3$ nanowires in arrays of open nanofluidic channels. *Sci. Rep.* **6**, 19834 (2016).
28. B. Náfrádi *et al.*, Optically switched magnetism in photovoltaic perovskite CH_3NH_3 (Mn:Pb)I_3. *Nat. Commun.* **7**, 13406 (2016).
29. M. Belmeguenai *et al.*, Temperature dependence of magnetic properties of $La_{0.7}Sr_{0.3}MnO_3/SrTiO_3$ thin films on silicon substrates. *Phys. Rev. B* **81**, 054410 (2010).
30. A. Pisoni *et al.*, Metallicity and conductivity crossover in white light illuminated $CH_3NH_3PbI_3$ perovskite. arXiv:1604.05637 [cond-mat] (19 April 2016).
31. A. M. Haghiri-Gosnet, J. P. Renard, CMR manganites: Physics, thin films and devices. *J. Phys. D Appl. Phys.* **36**, R127–R150 (2003).
32. A. Urushibara *et al.*, Insulator-metal transition and giant magnetoresistance in $La_{1-x}Sr_xMnO_3$. *Phys. Rev. B* **51**, 14103–14109 (1995).
33. G. Xing *et al.*, Long-range balanced electron- and hole-transport lengths in organic-inorganic $CH_3NH_3PbI_3$. *Science* **342**, 344–347 (2013).
34. M. H. Kryder *et al.*, Heat assisted magnetic recording. *Proc. IEEE* **96**, 1810–1835 (2008).
35. S. D. Stranks *et al.*, Electron-hole diffusion lengths exceeding 1 micrometer in an organometal trihalide perovskite absorber. *Science* **342**, 341–344 (2013).
36. P. Kaushal, S. Chand, J. Osvald, Current–voltage characteristics of Schottky diode simulated using semiconductor device equations. *Int. J. Electron.* **100**, 686–698 (2013).